International Journal of Computer Integrated Manufacturing

ISSN: 0951-192X (Print) 1362-3052 (Online) Journal homepage: www.tandfonline.com/journals/tcim20

Understanding and control of gas porosity in metal laser powder-bed fusion additive manufacturing

Robert Laskowski, Jakub Mikula & Guglielmo Vastola

To cite this article: Robert Laskowski, Jakub Mikula & Guglielmo Vastola (2025) Understanding and control of gas porosity in metal laser powder-bed fusion additive manufacturing, International Journal of Computer Integrated Manufacturing, 38:12, 1681-1696, DOI: 10.1080/0951192X.2025.2452984

To link to this article: https://doi.org/10.1080/0951192X.2025.2452984

INTERNATIONAL JOURNAL OF COMPUTER INTEGRATED MANUFACTURING
2025, VOL. 38, NO. 12, 1681–1696
https://doi.org/10.1080/0951192X.2025.2452984

Understanding and control of gas porosity in metal laser powder-bed fusion additive manufacturing

Robert Laskowski, Jakub Mikula and Guglielmo Vastola

Institute of High Performance Computing (IHPC), Agency for Science, Technology and Research (A*STAR), Singapore, Republic of Singapore

ABSTRACT

The presented study discusses mechanism leading to gass porosity formation during additive manufacturing (AM) process. The method employs numerical scheme, which includes fluid dynamics of the melt pool and on-the-fly ray-tracing implemented within a phase field framework where the liquid/vapor interface is captured within volume of fluid approach. The emission of pores in the middle or the stripe happens only for relatively low scan speed (less than 0.6 m/s for IN718). The stripe edges (laser turning points) are identified as potential source of gas pores at scan speeds as high as 1 m/s. Simulations of laser turning, representative of the edge of a stripe, suggest the way the process parameters can be altered to avoid local porosity formation, while still ensuring a deep melt pool suitable for high build rates. The laser power modulation around the edge can lead to over 50% reduction of the pores emission. The proposed numerical framework requires only moderate computational resources, thus providing a holistic tool to decrease defect density and thus further improve quality of additive manufactured components.

ARTICLE HISTORY
Received 30 January 2024
Accepted 8 January 2025

KEYWORDS
Laser powder-bed fusion; melt pool modeling; keyhole modeling; gas porosity

1. Introduction

Laser powder-bed fusion (L-PBF) additive manufacturing (AM) of metals is the process whereby a laser selectively scans thin layers of powder (typically with a thickness of 40 μm) according to an exposure strategy to reproduce a horizontal cross-section of the component to be built. By exposing each cross-section, layer by layer in a controlled environment, the component is ultimately built.

Past its pioneering development (Kruth et al. 2007) and early adoption (Weller, Kleer, and Piller 2015), L-PBF parts have become (https://doi.org/10.1016/j.jallcom.2021.158630cost-effective) solutions in applications such as spare parts replacements (Khajavi, Partanen, and Holmstrom 2014), complex geometries (Gao et al. 2015), medical implants (Kaur and Singh 2019), and aerospace components (Gisario et al. 2019).

Ubiquitous among its different applications, sectors and use cases, assurance of component quality is of paramount importance. Indeed, quality control in L-PBF is a particularly challenging task due to the complexity of the process, which is characterized by high energy density, fast fluid flow in the melt pool (Matthews et al. 2016), violent metal evaporation (Zheng et al. 2018) and ejection of spatters (Khairallah et al. 2016). As a result of this complex energy balance, defects, in the form of pores, are formed in the solidified material (du Plessis et al. 2018; Zhang, Li, and Bai 2017). There are two main types of defects, which correspond to two opposite operating regimes of the L-PBF process.

The first type of defect occurs at low energy density, below 80 J/mm^3 (Xu et al. 2022). In this regime, the heat input is insufficient to fully melt the powder. The melt pool is fully in conduction mode, and the outcome is not melted solid showing large lack-of-fusion pores (Tang, Chris Pistorius, and Jack 2017). Thanks to the large amount of work already done in this area, lack-of-fusion porosity is generally well understood; avoidance of this regime can be obtained by increasing the processing energy density, either by increasing laser power, decreasing scan speed or decreasing hatch spacing or layer thickness (Mukherjee and DebRoy 2018).

The second type of pores occurs at high energy density, greater than 110 J/mm^3 (Xu et al. 2022). Here, the highly localized heat input of the laser is sufficient to create strong, directional metal evaporation from the

CONTACT Robert Laskowski rolask@ihpc.a-star.edu.sg; Guglielmo Vastola vastolag@ihpc.a-star.edu.sg
This article has been corrected with minor changes. These changes do not impact the academic content of the article.

melt pool. Correspondingly, the recoil pressure generated by such vapor ejection pushes the liquid surface down, forming a distinctive keyhole. Importantly, the presence of a deep melt pool itself is not necessarily an issue; in fact, a melt depth of around three layer thicknesses (in other words, in the range of 150–200 μm) is indeed beneficial to process quality, ensuring good metallurgical bonding between the material being melt and the existing solid. However, upon a further increase of energy density, the indentation assumes the shape of a distinctive keyhole. In this regime, energy absorption becomes strongly influenced by the localized reflection and absorption of laser through the depth of the keyhole and the overall liquid surface. In-situ X-ray experiments (Cunningham et al. 2019) show the liquid surface is highly dynamic, exhibiting ripples that may pinch and, through this mechanism, emit bubbles which, if trapped by the advancing solid–liquid interface, become gas pores.

In response to its crucial role in gas porosity formation, computational modeling and simulation provides a powerful framework to investigate the mechanistic variables affecting keyhole stability and their role in the emission of gas pores. Through recent years, several efforts have significantly progressed our understanding of gas porosity formation. Historically, it is important to recognize the pioneering modeling work on deep penetration keyhole welding, which already showed the feasibility of a numerical scheme with explicit resolution of the keyhole together with ray-tracing capability to represent the laser source (Pang et al. 2010). In terms of L-PBF process, early work formulated semi-analytical models to quantify porosity and link it to energy density, where the heat source was a double cylinder to model the effect of the keyhole in melt pool depth and width (Vastola, Pei, and Zhang 2018). Later, computational models including fluid dynamics modeling as well as on-the-fly ray tracing were specifically developed. Using an Arbitrary Lagrangian-Eulerian finite element framework including ray-tracing, Khairallah *et al*. showed high fidelity simulations of single tracks, revealing the tight links between melt pool dynamics, keyhole, and liquid metal ejections (spatters) (Khairallah et al. 2016). Bayat *et al*. used the volume of fluid approach, coupled with ray tracing and applied to Ti6Al4V, showing bubble emission and flow in the melt pool (Bayat et al. 2019). Zakirov *et al*. developed an efficient scheme using volume of fluid approach leveraging on graphical processing units (Zakirov et al. 2020). In-situ X-ray imaging was recorded by Cunningham *et al*. (Cunningham et al. 2019) for stationary and moving laser cases; Wei *et al*. showed that bubble emissions from stationary keyhole could be rationalized using a phase field model using the Lattice Boltzmann method coupled with ray-tracing (Wei et al. 2022).

Key evidence was shown by Zhao *et al*. who reported high-speed in-situ measurements of the keyhole, proving its role in bubble emission (Zhao et al. 2020a). With direct correlation to similar X-ray in situ experiments, Wang *et al*. studied the influence of process parameters (scan speed) on keyhole depth and pores size (Wang et al. 2022, 2023). Martin *et al*. showed that the turning points of the laser (for instance, after each scan vector within a stripe of exposure) corresponds to a particularly challenging situation, where energy density locally increases and the probability of pore generation increases (Martin, Calta, Khairallah, Wang, Depond, Fong, Thampy, et al. 2019). Assisted by computational models including vapor plume, Gan *et al*. derived a scaling law that correlates process parameters with volume fraction of gas pores, showing consistency among the main materials systems of Ti64, IN718, and SS316L (Gan et al. 2021). Additional experiments and modeling in Huang *et al*. detailed the delicate balance between front and rear surface of the keyhole in respect to laser scan direction and detailed the temporal evolution of bubbles from initial enlargement to partial collapse (Huang et al. 2022a). The role of argon and metallic vapor flows was explicitly studied by Leung *et al*. (Leung et al. 2022), where a multi phase model was developed using OpenFOAM software library, and the transition from 'I' to 'J' shape of the keyhole was correlated to gas porosity formation.

Clearly, the existing body of work has demonstrated a link between the presence of the keyhole and gas pores formation. At the same time, the mechanistic sequence of events that lead to bubble emissions has not been fully resolved. Zhao *et al*. discussed that the key step of bubble detachment can be triggered by localized shock waves (Zhao et al. 2020a). However, Wang *et al*. pointed out that the shock waves can play a key role in splitting the bubbles, while may not necessarily be the triggers to emission (Wang et al. 2022). Conversely, Ren *et al*. showed that protrusions within the front keyhole wall are temporally correlated to keyhole pinching (Ren et al. 2023a), suggesting a link between the

two. Finally, Guo *et al*. confirmed the complexity of gas porosity formation, identifying three different mechanisms that could lead to bubble emission (L. Guo et al. 2023).

With an holistic assessment, the current body of work clearly shows that a detailed understanding of keyhole bubble emission still remains elusive, without a conclusive cause-and-effect mechanism that could clearly connect a keyhole-shaped melt pool to the emission of gas bubbles. This work establishes such connection providing details of the pore pinching mechanism by numerical simulations. The applied numerical framework is based on fluid dynamics, coupled with on-the-fly ray tracing and the phase field method (PFM). Using such numerical scheme, the simulations require only moderate computational resources while revealing the mechanism of melt pool surface instability. The presented results corroborate the evidence seen in experiments by Ren *et al*. in identifying local surface protrusions as the fundamental key initiator to bubble emission. Equipped with this model, the challenge of gas porosity formation at the turning points of scan vectors (Martin, Calta, Khairallah, Wang, Depond, Fong, Thampy, et al. 2019) is revisited. It is identified that gas pores can be suppressed by an appropriate change of process parameters as the laser approaches the turning points. In turn, such results could have important consequences in achieving stable and deep melt pools, which in turn is key requisite to achieve high build rate additive manufacturing.

2. Methodology

This study aims to describe the mechanisms of gas pore formation through numerical simulations. Understanding these mechanisms enables the development of strategies to control gas porosity in metal laser powder bed fusion additive manufacturing. The applied computational framework follows in large extend Ref (Laskowski et al. 2022). However, this work implements volume of fluid (VOF) method of Körner *et al*. (Körner et al. 2005), which allows for a precise definition of an interface between gas and the solid or liquid phases. This scheme simplifies implementation of the phase field model and thermal solver, allowing them to operate within volume occupied by liquid or solid without a need for vapor order parameter in comparison to the 'diffuse liquid/vapor interface' approach used in Ref (Laskowski et al. 2022). As a result, the liquid/vapor interface evolves only by melt pool flow. Lattice Boltzmann method (LBM) is used for that purpose. However, as a consequence, a special care must be exercises in the evaluation of the curvature of the liquid/vapor interface determining surface tension term in melt pool flow solver. The melting and solidification processes are simulated using phase field method, which introduces diffuse interface between liquid and solid phases and following formulation proposed by Moelans *et al*. (Moelans, Blanpain, and Wollants 2008). In such configuration of the phase field model, the gas pores are detected by recursive algorithm, searching for clusters of empty (no solid or liquid) grid points not connected to the space above powder bed. In order to properly tract pores volume, an ideal gas relation between the volume, pressure and temperature inside the pore is assumed. The details of the implementation are provided in Appendix A.

Material studied in this work is Nickel super-alloy IN718. The material and model parameters are collected in Table B1 in Appendix B. The powder is distributed using a rain drop algorithm in which the particles are seeded at random positions and allowed to fall into a local minima one after another. The parameters of the powder such as particle size, shape, and composition are taken from Q. B. Nguyen *et al*. (Nguyen et al. 2017). The particles radii follow a bi-normal distribution with peak at $25.5 \times 10^{-6}m$ and square root of left and right variances of $\sigma_L = 2 \times 10^{-6}m$ and $\sigma_R = 10^{-5}m$.

The representative volume element (RVE) used in this work allows to approximate the laser path near an edge of a stripe, as shown in Figure 1. At the current stage simulations of the whole width of the stripe would be numerically difficult; therefore, RVE focuses on its fragment. The length, width and height of the RVE is set to 3 mm, 0.75 mm and 1.0 mm, respectively. The thickness of the solid substrate is set to 0.75 mm, which is covered by 0.04 mm powder layer, the remaining of the high of RVE is considered as an empty region (no phase assigned). The laser path consist of two lines 2.7 mm long. Line '1' starts at the left edge of RVE and ends 0.3 mm from the right edge of the RVE. Line '2' starts at 0.3 mm from the right edge and ends at the left edge. The lines are

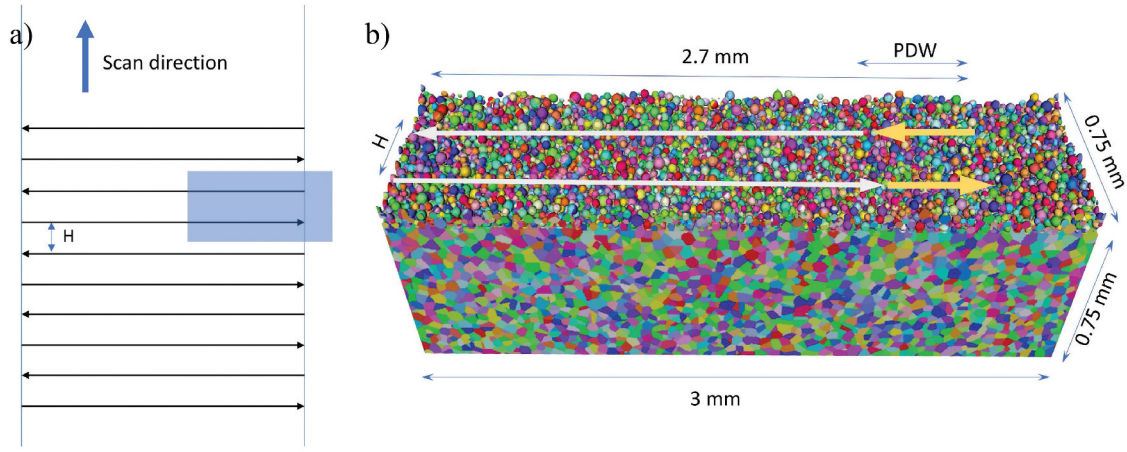

Figure 1. RVE representing the right edge of a stripe: (a) fragment of a scan pattern composed of two lines separated by hatch spacing (H). The first line starts at the left side of the RVE and ends at 0.3 mm from its right side. The direction of the second line is reversed. PDW indicates a width of a segment of a line where the power for some of the presented calculations is linearly decreasing (first line) or increasing (second line).

separated by the hatch spacing (H). The computational details are provided inAppendix C.

The discussion presented in this work focused on the formation of gas pores in melt pool, which may eventually contribute to an overall porosity after solidification. It is already known that gas pores originate from the keyhole collapse (Huang et al. 2022b; Martin, Calta, Khairallah, Wang, Depond, Fong, Thampy, et al. 2019; Ren et al. 2023b; Wang et al. 2022; Zhao et al. 2020b). Zhao *et al*. (Zhao et al. 2020b) investigated condition for keyhole formation in respect to laser power and scan velocity, disclosing relation between threshold laser power and scan velocity. Martin *et al*. (Martin, Calta, Khairallah, Wang, Depond, Fong, Thampy, et al. 2019) indicated a role of laser tract turn point in the formation of keyhole pores. The presented RVE and computational methodology allows us to discus these points in more detail.

The keyhole shape and gas pores formation through that are dependent on the laser beam size. Usually a narrow beam would more likely generate gas pores. In this work, however, we consider a standard laser beam size (4σ) of 100 μm used in the previously reported measurements of porosity (Laskowski et al. 2022). The laser beam is modeled by ray-tracing method. The number of rays is equal to 10^4. The rays are randomly distributed following Gaussian distribution with $\sigma = 25\mu m$.

3. Results and discussion

The effect of process parameters on porosity in IN718 reported in Ref Laskowski et al. (2022) indicate that the keyhole gas pores appear for samples printed with laser power of 286 W and scan velocity of 0.75 m/s. However, according to our calculations (Figure 2) at such scan speed, keyhole pores do not appear, assuming single line track and laser power up to 500 W. The threshold velocity is estimated to be around 0.6–0.7m/s, which as can be seen in Figure 2, compiles simulation results for single track performed for

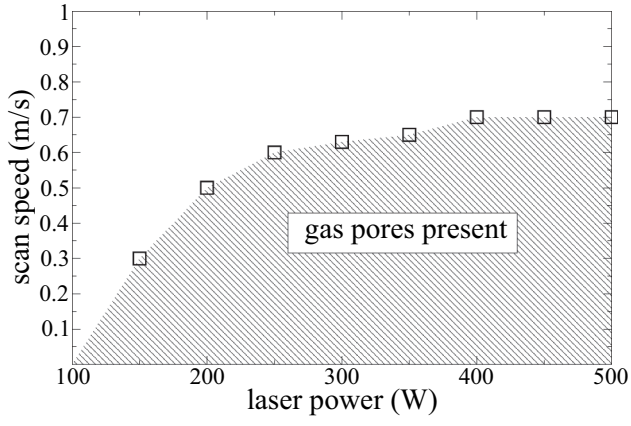

Figure 2. The laser power vs. scan speed threshold for key-hole gas pores seeding estimated using simulations of the single line (line 1) RVE from fig. 1.

values of laser power in range 100–500 W and scan speed from 0.1 to 1 m/s, estimating a threshold at which gas pores appear in power/speed space. This observation can be understood comparing keyhole shape for two scans with speed 0.5 m/s and 0.75 m/s, presented in Figure 3. The keyhole appearing for scan with velocity of 0.5 m/s is considerably deeper and more narrow, offering suitable conditions for pores formation. Figure 4 presents a sequence of snapshots depicting mechanism of pore formation. In Figure 4a, at time t_0, a small 'ripple' is formed in the form of open ring on the front and side walls of the keyhole. The plane of the ring is oriented at roughly 30° to 60° with respect to laser beam direction. This observation is consistent with the protrusions reported in Ren et al. (2023b). The sequence of Figure 4b-d shows clearly the ring traveling down the key hole and increasing its width at the same time. It eventually closes off the keyhole tip (Fig. 4e). The top wall of just closed pore is pushed down by the high recoil pressure. Under such conditions, there is a probability that the wall may break; however, if it stays intact, the pore travels along the bottom of the melt pool towards its tail. The closure of the keyhole is possible only when the front and back walls form an angle smaller than the orientation of the ripple ring. As we have seen in Figure 3 for the 0.75 m/s scan, this angle is quite large, such that the plane of the open ring (protrusion) traveling down the key hole is parallel to the back wall. In such situation, closure of the open ring is geometrically impossible. Figure 5 summarizes presented observation in a more schematic manner. The presented picture clearly resembles a wave generated by a localized perturbation traveling on the melt pool surface pushed by the recoil pressure: on a flat surface, it would form a cone,

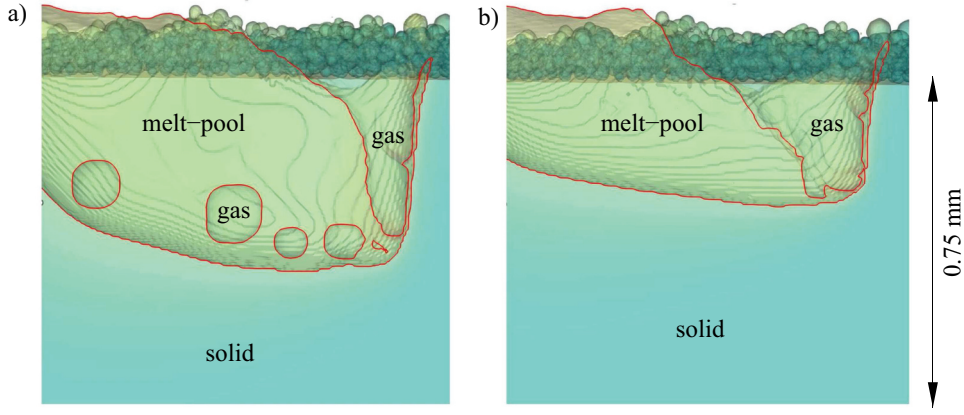

Figure 3. Key hole cross-section registered for laser scan velocity of (a) 0.5m/s and (b) 0.75m/s. The red line separates vapor or solid region from melt pool.

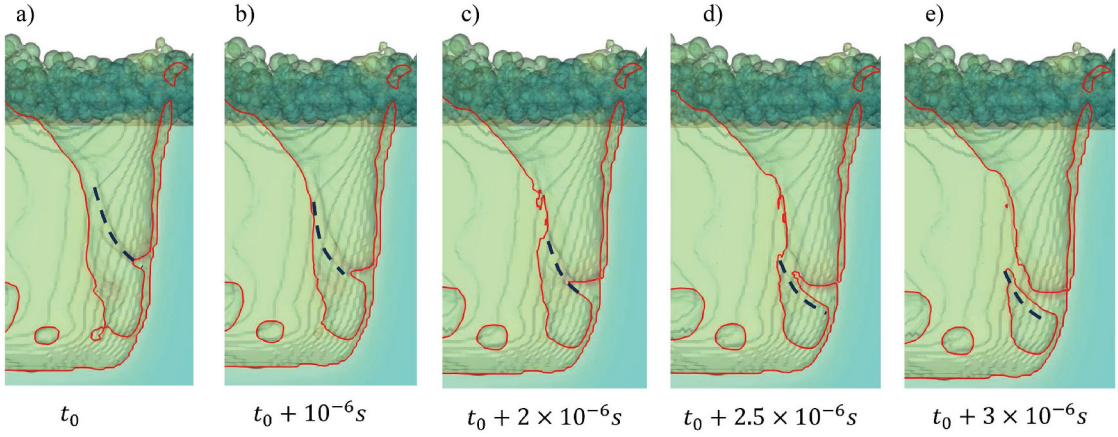

Figure 4. The gas pore formation process for scan velocity of 0.5 m/s and laser power 500 W. (a) Protrusion nucleates at the wall of keyhole at time t_0. (b-d) Protrusion grows traveling down the keyhole. (e) Protrusion closes and gas-pore forms at $t_0 + 3 \times 10^{-6}s$.

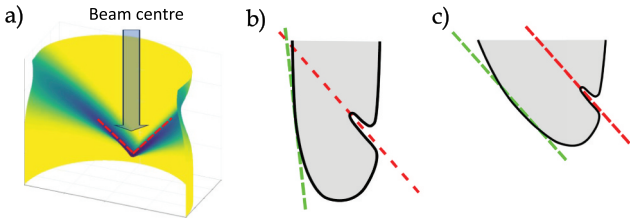

Figure 5. (a) Schematic of a ripple formed at the front wall of the key hole. The red dashed lines indicate the inclination of the ripple plane around the center of the laser beam on the front of the key hole. (b) Schematic of the key hole shape at low laser velocity. The dashed lines indicate the orientation of the ripple plane and the back wall of the key hole. The planes intersects and the ripple grow leads to pinching the key hole. (c) Schematic of the key hole at large laser speed. The ripple plane is parallel to the back wall of the key hole. The pinching is not possible in this situation.

while on the wrapped keyhole surface, it forms a ring. The position of the initial 'ripple' appears at the position of the highest laser power density (for a Gaussian-shaped beam).

The mechanism proposed by Martin *et al.* (Martin, Calta, Khairallah, Wang, Depond, Fong, Thampy, et al. 2019) can be used to explain actual gas porosity observed for higher scan velocity. In this case, key hole shape become preferable for formation of the gas pores for a short time around the turnnd points of the stripe. This scenario is captured in Fig. 6, where melt pool is visualized along path imitating the right edge of a stripe for scan speed of 0.75 m/s, laser power of 400 W and hatch spacing of 0.08 mm. Points A, B a C mark position of the laser beam along 'line 1' incoming towards the edge of the stripe. Points D, E and F mark the beam position along line leaving the edge. As can be seen in Figure 6 for all the snapshots except D (the first after the turn), key hole shape does not allow the gas pore formations, as the back wall is at high angle to the front. For the snapshot D, the keyhole is narrow and the pores are being seeded. The seeding process continues at distance roughly 0.5 mm from the stripe edge, until keyhole regains its equilibrium shape.

Pores volume accumulated during scan along the path for scan velocity of 0.5 m/s, 0.75 m/s, 1.0 m/s and various laser power are presented in Figure 7. Note that the pores volume is quite sensitive to scan velocity, effectively it drops by an order of magnitude with velocity increment of 0.25 m/s. As expected for velocity 0.5 m/s in Figure 7a, considerable pores volume is generated in the line incoming to the turn point ('line 1'). The time for completion of a single line is used as a scale in Figure 7, such that '1' on time axis marks the turn point. It may seem that the pores are generated within the first half of the line pass. However we noticed that some

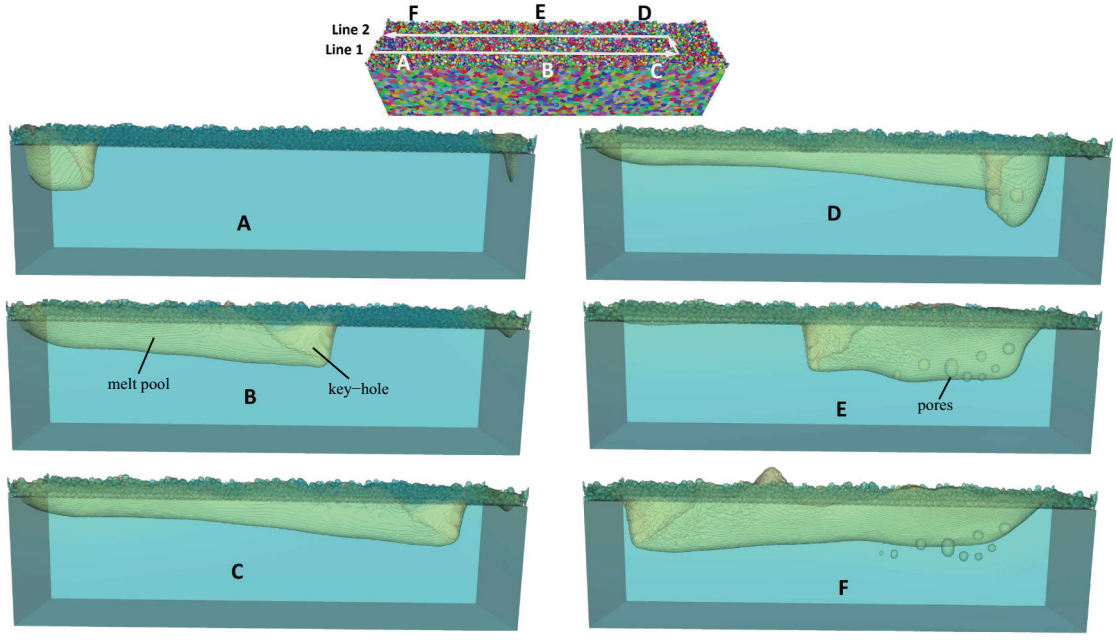

Figure 6. The melt pool state displayed along the scan path shown at the top of the figure (scan speed of 0.75 m/s and laser power of 400 W and hatch spacing of 0.08 mm). Points A, B, C are along the line 1 (before turn point). Points D, E, F are along line 2 (after turn point). Note accumulation of gas pores near point D (vicinity of stripe edge).

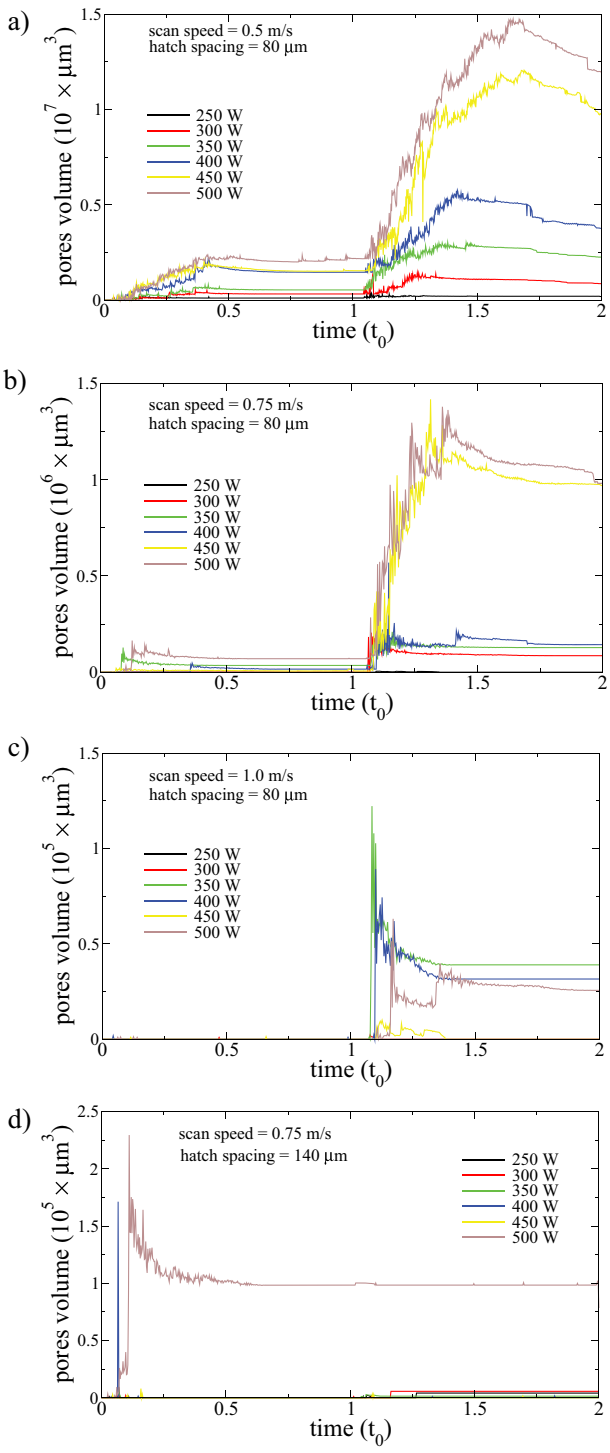

Figure 7. The total gas pore volume accumulated along the scan path for selected values of laser power. The boundary temperature T_b is kept at 600 K, the hatch spacing is equal to 0.08 mm for (a-c), where the scan speed is equal to (a) 0.5 m/s, (b) 0.75 m/s, (c) 1.0 m/s. For (d), the hatch spacing is equal to 0.14 mm and the scan speed is 0.75 m/s. The scale of the time axis t_0 is equal to pass time for the line 1.

of the pores may reach the melt pool surface and got annihilated; at the same time, new ones detach from the keyhole. The pores volume dramatically increases after the turn points, roughly by factor of 5 for high laser power. The results computed for scan with velocity 0.75 m/s show nearly negligible volume generated along 'line 1' mostly at the initial stage close to the left edge of the RVE. Therefore more dramatic increase of pore volume after the turn point is observed. Figure 7c shows results for scan speed of 1 m/s; in this case, no pores are generated during passing the first line. Comparing to the other two cases, here roughly half of the pores generated after the turn point are annihilated. Another factor worth noting is the effect of hatch spacing (H). The results presented in Fig. 7(a-c) have been generated assuming that H is equal to 0.08 mm. Figure 7(d) shows the results for H = 0.14 mm and scan speed 0.76 m/s. As seen there, the turn point effect nearly disappeared, suggesting that for such large spacing, the lines become independent. This is rather understandable considering the laser beam diameter 4σ used in the simulation of 100 μm is significantly smaller than 140 μm of the hatch spacing. Under this conditions, the lack of fusion (LOF) porosity becomes apparent. The strong dependence of the gas porosity on the hatch spacing has been seen in reported measurements (Laskowski et al. 2022).

Due to the nature of the computational methodology employed in this work, it is not trivial to couple the RVE to the rest of the volume at a part scale. Such coupling would require an information related to the part shape and the detains of scan pattern at this scale. In this work, a simplified approach is applied, where a single value of temperature (T_b) describes initial and boundary conditions at the bottom and sides parallel to the scan vector of the RVE (the details of the actual implementation are provided in the appendix). Figure 8 shows the effect T_b on the pore volume generated during scans with velocity 0.75 m/s and laser power of 500 W. The trend seems non monotonic. The maximum value is reached for T_b equal to 500 K. Very low T_b equal to 300 K results in lower pore volume. This result suggest a possible

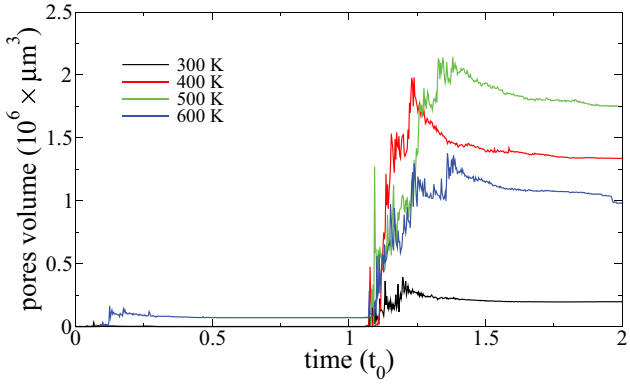

Figure 8. The total gas pore accumulated along scan path computed for different values of the boundary temperature T_b. Scan speed was set to 0.75 m/s, hatch spacing is equal to 0.08 mm and laser power is equal to 500 W.

variation of the pore volume density across a build, dependent of the actual thermal conditions around the scan region represented by the RVE used in this work.

Figure 6 shows that most of the pores are located close to the bottom of the melt pool, indicating that it would be impossible to remove them by remelting after re-coating. Therefore another approach may be required to decrease the pore volume. A simple scheme relying on gradually decreasing laser power before the turn point and increasing it back to a nominal value when moving away from the turn point has been tested in this work. Figure 9a shows the results for nominal power (in the middle of the stripe) of 500 W and the power at turn point of 250 W (scan speed of 0.75 m/s, hatch spacing of 0.08 mm and boundary temperature T_b equal to 600 K). The length of the path portion where the power is linearly decreasing (PWD) is varied between 0 and 0.9 mm. The simulations show that increment of PWD from 0 mm to 0.3 mm nearly doubles pore volume registered at the completion if the second line (black and red lines in Figure 9, $t_0 = 2$) increases from $10^6 \mu m^3$ to $2 \times 10^6 \mu m^3$. Further increment of PWD value to 0.6 mm and 0.9 mm leads to gradual decrease in the pore volume to $0.6 \times 10^6 \mu m^3$ and $0.3 \times 10^6 \mu m^3$, respectively. Figure 9b summarizes this observation in graphical form.

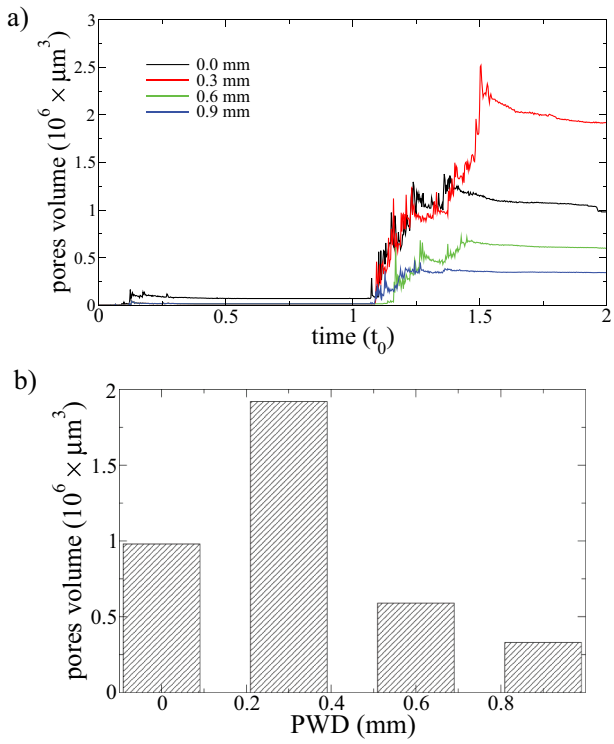

Figure 9. (a) The total gas pore volume accumulated along scan path computed for varying value of power decline width (PWD in Figure 1). Laser power is set to 500 W at the inner portion of the path and decreased to 250 W at the right edge of the scan path. The hatch spacing is kept at 0.08 mm, boundary temperature T_b is set to 600 K and scan speed is 0.75 m/s. (b) summarizes the pore volume after completion of the path for different values of PWD.

4. Conclusions

The numerical scheme presented in this work responds to industry's need for accurate and fast modeling of gas porosity in metal additive manufacturing. It offers multi physics approach taking into consideration solid–liquid phase transition, melt pool and heat flows. The implementation is based on the multi phase field method where fluid dynamics as well as ray-tracing are co-solved on the fly. Application of such scheme to study single and two-track scan vectors has revealed the details of the complex process of powder melting, dynamic keyhole formation, keyhole surface instability and generation of gas bubbles. At the current stage of the development of numerical approaches for additive manufacturing at powder

scale, the presented scheme delivers a unique study showing the microsecond-sequence of events that lead to bubble emission. The results provide a direct understanding and explanation of the evidence brought forward by experiments of Ren *et al*. (Ren et al. 2023b), proving that the local rippling of the front-facing keyhole surface is the key initiator. However, the results indicate that the gas pores are not seeded for single track scan with velocity higher then 0.7 m/s, which is well below typical process parameter. The presence of the gas pores for higher scan speed is explained by presented simulations of the scan path close to the edge of a stripe, i.e. laser scan turning point. The presented simulations directly show that the key-hole around this point assumes shape that allows pore seeding. This visualizes the effect observed experimentally for Ti-6Al04V alloy (Martin, Calta, Khairallah, Wang, Depond, Fong, Thampy, et al. 2019). Those simulations leads to proposal for modifying the process parameters to avoid such detrimental effect, while keeping the melt pool as deep as possible. The quantitative recipe has the vision of enabling stable, deeper melt pools to achieve higher build rates and thus further promote adoption of additive manufacturing in industrial, cost-effective applications.

Disclosure statement

No potential conflict of interest was reported by the author(s).

Funding

This work was supported by the Agency for Science, Technology and Research (A*STAR) with Grants "Advanced Models for Additive Manufacturing (AM2)" (M22L2b0111) and "Metal AM Powders: Reusability, Rejuvenation, Cost, Quality & Performance (RRAMP)" (M22K7a0047). Any opinions, findings and conclusions or recommendations expressed in this material are those of the author(s) and do not reflect the views of A*STAR.Computational resources are gratefully acknowledged from the A*STAR Computational Resource Center as well as from the National Supercomputing Center Singapore (NSCC).

Data availability statement

The raw data that support the findings of this study are available from the corresponding authors.

References

Bayat, M., A. Thanki, S. Mohanty, A. Witvrouw, S. Yang, J. Thorborg, N. Skat Tiedje, and J. Henri Hattel. 2019. "Keyhole-Induced Porosities in Laser-Based Powder Bed Fusion (L-PBF) of Ti6Al4V: High-Fidelity Modelling and Experimental Validation." *Additive Manufacturing* 30:100835. https://doi.org/10.1016/j.addma.2019.100835.

Chatterjee, S., and N. Moelans. 2021. "A Grand-Potential Based Phase-Field Approach for Simulating Growth of Intermetallic Phases in Multicomponent Alloy Systems." *Acta Materialia* 206:116630. https://doi.org/10.1016/j.actamat.2021.116630.

Chen, H., C. Teixeira, and K. Molvig. 1998. "Realization of Fluid Boundary Conditions via Discrete Boltzmann Dynamics." *International Journal of Modern Physics C* 9 (08): 1281–1292. https://doi.org/10.1142/S0129183198001151.

Cho, J.-H., and S.-J. Na. 2006. "Implementation of Real-Time Multiple Reflection and Fresnel Absorption of Laser Beam in Keyhole." *Journal of Physics D: Applied Physics* 39 (24): 5372–5378. https://doi.org/10.1088/0022-3727/39/24/039.

Cunningham, R., C. Zhao, N. Parab, C. Kantzos, J. Pauza, K. Fezzaa, T. Sun, and A. D. Rollett. 2019. "Keyhole Threshold and Morphology in Laser Melting Revealed by Ultrahigh-Speed X-Ray Imaging." *Science* 363 (6429): 849–852. https://doi.org/10.1126/science.aav4687.

d'Humières, D., and I. Ginzburg. 2009. "Viscosity Independent Numerical Errors for Lattice Boltzmann Models: From Recurrence Equations to "Magic" Collision Numbers." *Computers & Mathematics with Applications* 58 (5): 823–840. Mesoscopic Methods in Engineering and Science. https://doi.org/10.1016/j.camwa.2009.02.008.

Dong, H. B., and P. D. Lee. 2005. "Simulation of the Columnar-To-Equiaxed Transition in Directionally Solidified Al–Cu Alloys." *Acta Materialia* 53 (3): 659–668. https://doi.org/10.1016/j.actamat.2004.10.019.

du Plessis, I. Y. Anton, I. Yadroitsava, and S. G. Le Roux. 2018. "X-Ray Microcomputed Tomography in Additive Manufacturing: A Review of the Current Technology and Applications." *3D Printing and Additive Manufacturing* 5 (3): 227–247. https://doi.org/10.1089/3dp.2018.0060.

Gan, Z., O. L. Kafka, N. Parab, C. Zhao, L. Fang, O. Heinonen, T. Sun, and W. Kam Liu. 2021. "Universal Scaling Laws of Keyhole Stability and Porosity in 3D Printing of Metals." *Nature Communications* 12 (1): 2379. https://doi.org/10.1038/s41467-021-22704-0.

Gandin, C. A., M. Rappaz, and R. Tintillier. 1994. "3-Dimensional Simulation of the Grain Formation in Investment Castings." *Metallurgical and Materials Transactions A* 25 (3): 629–635. https://doi.org/10.1007/BF02651604.

Gao, W., Y. Zhang, D. Ramanujan, K. Ramani, Y. Chen, C. B. Williams, C. C. L. Wang, Y. C. Shin, S. Zhang, and P. D. Zavattieri. 2015. "The Status, Challenges, and Future of Additive Manufacturing in Engineering." *Computer-Aided Design* 69:65–89. https://doi.org/10.1016/j.cad.2015.04.001.

Ginzburg, I., F. Verhaeghe, and D. d'Humiéres. 2008 a. "Study of Simple Hydrodynamic Solutions with the Two-Relaxation-

Times Lattice Boltzmann Scheme." *Communications in Computational Physics* 3 (3): 519–581.

Ginzburg, I., F. Verhaeghe, and D. d'Humiéres. 2008 b. "Two-Relaxation-Time Lattice Boltzmann Scheme: About Parametrization, Velocity, Pressure and Mixed Boundary Conditions." *Communications in Computational Physics* 3 (2): 427–478.

Gisario, A., M. Kazarian, F. Martina, and M. Mehrpouya. 2019. "Metal Additive Manufacturing in the Commercial Aviation Industry: A Review." *Journal of Manufacturing Systems* 53:124–149. https://doi.org/10.1016/j.jmsy.2019.08.005.

Guo, L., H. Wang, H. Liu, Y. Huang, Q. Wei, C. Lun Alex Leung, Y. Wu, and H. Wang. 2023. "Understanding Keyhole Induced-Porosities in Laser Powder Bed Fusion of Aluminum and Elimination Strategy." *International Journal of Machine Tools & Manufacture* 184:103977. https://doi.org/10.1016/j.ijmachtools.2022.103977.

Guo, Z., B. Shi, and N. Wang. 2000. "Lattice BGK Model for Incompressible Navier–Stokes Equation." *Journal of Computational Physics* 165 (1): 288–306. https://doi.org/10.1006/jcph.2000.6616.

He, X., Q. Zou, L.-S. Luo, and M. Dembo. 1997. "Analytic Solutions of Simple Flows and Analysis of Nonslip Boundary Conditions for the Lattice Boltzmann BGK Model." *Journal of Statistical Physics* 87 (1–2): 115–136. https://doi.org/10.1007/BF02181482.

Heulens, J., B. Blanpain, and N. Moelans. 2011. "A Phase Field Model for Isothermal Crystallization of Oxide Melts." *Acta Materialia* 59 (5): 2156–2165. https://doi.org/10.1016/j.actamat.2010.12.016.

Huang, Y., T. G. Fleming, S. J. Clark, S. Marussi, K. Fezzaa, J. Thiyagalingam, C. Lun Alex Leung, and P. D. Lee. 2022a. "Keyhole Fluctuation and Pore Formation Mechanisms During Laser Powder Bed Fusion Additive Manufacturing." *Nature Communications* 13 (1): 1170. https://doi.org/10.1038/s41467-022-28694-x.

Huang, Y., T. G. Fleming, S. J. Clark, S. Marussi, K. Fezzaa, J. Thiyagalingam, C. Lun Alex Leung, and P. D. Lee. 2022b. "Keyhole Fluctuation and Pore Formation Mechanisms During Laser Powder Bed Fusion Additive Manufacturing." *Nature Communications* 13 (1). https://doi.org/10.1038/s41467-022-28694-x.

Kaur, M., and K. Singh. 2019. "Review on Titanium and Titanium Based Alloys as Biomaterials for Orthopaedic Applications." *MATERIALS SCIENCE and ENGINEERING C-MATERIALS for BIOLOGICAL APPLICATIONS* 102:844–862. https://doi.org/10.1016/j.msec.2019.04.064.

Khairallah, S. A., A. T. Anderson, A. Rubenchik, and W. E. King. 2016. "Laser Powder-Bed Fusion Additive Manufacturing: Physics of Complex Melt Flow and Formation Mechanisms of Pores, Spatter, and Denudation Zones." *Acta Mat* 108:36–45. https://doi.org/10.1016/j.actamat.2016.02.014.

Khajavi, S. H., J. Partanen, and J. Holmstrom. 2014. "Additive Manufacturing in the Spare Parts Supply Chain." *Computers in Industry* 65 (1): 50–63. https://doi.org/10.1016/j.compind.2013.07.008.

Körner, C., M. Thies, T. Hofmann, N. Thürey, and U. Rüde. 2005. "Lattice Boltzmann Model for Free Surface Flow for Modeling Foaming." *Journal of Statistical Physics* 121 (1–2): 179–196. https://doi.org/10.1007/s10955-005-8879-8.

Krüger, T., H. Kusumaatmaja, A. Kuzmin, O. Shardt, G. Silva, and E. Magnus Viggen. 2017. *The Lattice Boltzmann Method Principles and Practice*. Switzerland: Springer International Publishing.

Kruth, J.-P., G. Levy, F. Klocke, and T. H. C. Childs. 2007. "Consolidation Phenomena in Laser and Powder-Bed Based Layerered Manufacturing." *Annals of the CIRP* 56 (2): 730. https://doi.org/10.1016/j.cirp.2007.10.004.

Ladd, A. J. C. 1994. "Numerical Simulations of Particulate Suspensions via a Discretized Boltzmann Equation. Part 1. Theoretical Foundation." *Journal of Fluid Mechanics* 271:285–309. https://doi.org/10.1017/S0022112094001771.

Laskowski, R., R. Ahluwalia, G. Teh Wei Hock, C. Sing Ying, C.-N. Sun, P. Wang, D. Tan Cheng Cheh, N. Mui Ling Sharon, G. Vastola, and Y.-W. Zhang. 2022. "Concurrent Modeling of Porosity and Microstructure in Multilayer Three-Dimensional Simulations of Powder-Bed Fusion Additive Manufacturing of INCONEL 718." *Additive Manufacturing* 60:103266. https://doi.org/10.1016/j.addma.2022.103266.

Leung, C. L. A., D. Luczyniec, E. Guo, S. Marussi, R. C. Atwood, M. Meisnar, B. Saunders, and P. D. Lee. 2022. "Quantification of Interdependent Dynamics During Laser Additive Manufacturing Using X-Ray Imaging Informed Multi-Physics and Multiphase Simulation." *Advanced Science* 9 (36): 2203546. https://doi.org/10.1002/advs.202203546.

Martin, A. A., N. P. Calta, S. A. Khairallah, J. Wang, P. J. Depond, A. Y. Fong, and V. Thampy, et al. 2019. "Dynamics of Pore Formation During Laser Powder Bed Fusion Additive Manufacturing." *Nature Communications* 10 (1): 1987. https://doi.org/10.1038/s41467-019-10009-2.

Martin, A. A., N. P. Calta, S. A. Khairallah, J. Wang, P. J. Depond, A. Y. Fong, and V. Thampy, et al. 2019. "Dynamics of Pore Formation During Laser Powder Bed Fusion Additive Manufacturing." *Nature Communications* 10 (1). https://doi.org/10.1038/s41467-019-10009-2.

Matthews, M. J., G. Guss, S. A. Khairallah, A. M. Rubenchik, P. J. Depond, and W. E. King. 2016. "Denudation of Metal Powder Layers in Laser Powder Bed Fusion Processes." *Acta Materialia* 114:33–42. https://doi.org/10.1016/j.actamat.2016.05.017.

Moelans, N., B. Blanpain, and P. Wollants. 2008. "Quantitative Analysis of Grain Boundary Properties in a Generalized Phase Field Model for Grain Growth in Anisotropic Systems." *Physical Review B* 78 (2): 024113. https://link.aps.org/doi/10.1103/PhysRevB.78.024113.

Mukherjee, T., and T. DebRoy. 2018. "Mitigation of Lack of Fusion Defects in Powder Bed Fusion Additive Manufacturing." *Journal of Manufacturing Processes* 36:442–449. https://doi.org/10.1016/j.jmapro.2018.10.028.

Nguyen, Q. B., M. Ling Sharon Nai, Z. Zhu, C.-N. Sun, J. Wei, and W. Zhou. 2017. "Characteristics of Inconel Powders for

Powder-Bed Additive Manufacturing." *Engineering* 3 (5): 695–700. https://doi.org/10.1016/J.ENG.2017.05.012.

Noble, D. R., and J. R. Torczynski. 1998. "A Lattice-Boltzmann Method for Partially Saturated Computational Cells." *International Journal of Modern Physics C* 9 (08): 1189–1201. https://doi.org/10.1142/S0129183198001084.

Pang, S., L. Chen, J. Zhou, Y. Yin, and T. Chen. 2010. "A Three-Dimensional Sharp Interface Model for Self-Consistent Keyhole and Weld Pool Dynamics in Deep Penetration Laser Welding." *Journal of Physics D: Applied Physics* 44 (2): 025301. https://doi.org/10.1088/0022-3727/44/2/025301.

Radhakrishnan, B., S. B. Gorti, J. A. Turner, R. Acharya, J. A. Sharon, A. Staroselsky, and T. El-Wardany. 2019. "Phase Field Simulations of Microstructure Evolution in IN718 Using a Surrogate Ni–Fe–Nb Alloy During Laser Powder Bed Fusion." *Metals* 9 (1): 14. https://doi.org/10.3390/met9010014.

Ren, Z., L. Gao, S. J. Clark, K. Fezzaa, P. Shevchenko, A. Choi, W. Everhart, A. D. Rollett, L. Chen, and T. Sun. 2023a. "Machine Learning–Aided Real-Time Detection of Keyhole Pore Generation in Laser Powder Bed Fusion." *Science* 379 (6627): 89–94. https://www.science.org/doi/abs/10.1126/science.add4667.

Ren, Z., L. Gao, S. J. Clark, K. Fezzaa, P. Shevchenko, A. Choi, W. Everhart, A. D. Rollett, L. Chen, and T. Sun. 2023b. "Machine Learning–Aided Real-Time Detection of Keyhole Pore Generation in Laser Powder Bed Fusion." *Science* 379 (6627): 89–94. https://doi.org/10.1126/science.add4667.

Steinbach, I. 2009. "Phase-Field Models in Materials Science." *Modelling and Simulation in Materials Science and Engineering* 17 (7): 073001. https://doi.org/10.1088/0965-0393/17/7/073001.

Strack, O. E., and K. C. Benjamin. 2007. "Three-Dimensional Immersed Boundary Conditions for Moving Solids in the Lattice-Boltzmann Method." *International Journal for Numerical Methods in Fluids* 55 (2): 103–125. https://doi.org/10.1002/fld.1437.

Tan, W., N. S. Bailey, and Y. C. Shin. 2013. "Investigation of Keyhole Plume and Molten Pool Based on a Three-Dimensional Dynamic Model with Sharp Interface Formulation." *Journal of Physics D: Applied Physics* 46 (5): 055501. https://doi.org/10.1088/0022-3727/46/5/055501.

Tang, M., P. Chris Pistorius, and L. B. Jack. 2017. "Prediction of Lack-Of-Fusion Porosity for Powder Bed Fusion." *Additive Manufacturing* 14:39–48. https://doi.org/10.1016/j.addma.2016.12.001.

Vastola, G., Q. X. Pei, and Y.-W. Zhang. 2018. "Predictive Model for Porosity in Powder-Bed Fusion Additive Manufacturing at High Beam Energy Regime." *Additive Manufacturing* 22:817–822. https://doi.org/10.1016/j.addma.2018.05.042.

Wang, L., Q. Guo, L. Chen, and W. Yan. 2023. "In-Situ Experimental and High-Fidelity Modeling Tools to Advance Understanding of Metal Additive Manufacturing." *International Journal of Machine Tools & Manufacture* 193:104077. https://doi.org/10.1016/j.ijmachtools.2023.104077.

Wang, L., Y. Zhang, H. Yi Chia, and W. Yan. 2022. "Mechanism of Keyhole Pore Formation in Metal Additive Manufacturing." *Npj Computational Materials* 8 (1): 22. https://doi.org/10.1038/s41524-022-00699-6.

Wei, M., W. Jun Ding, G. Vastola, and Y.-W. Zhang. 2022. "Quantitative Study on the Dynamics of Melt Pool and Keyhole and Their Controlling Factors in Metal Laser Melting." *Additive Manufacturing* 54:102779. https://doi.org/10.1016/j.addma.2022.102779.

Weller, C., R. Kleer, and F. T. Piller. 2015. "Economic Implications of 3D Printing: Market Structure Models in Light of Additive Manufacturing Revisited." *International Journal of Production Economics* 164:43–56. https://doi.org/10.1016/j.ijpe.2015.02.020.

Xu, J., Z. Wu, J. Niu, Y. Song, C. Liang, K. Yang, Y. Chen, and Y. Liu. 2022. "Effect of Laser Energy Density on the Microstructure and Microhardness of Inconel 718 Alloy Fabricated by Selective Laser Melting." *CRYSTALS* 12 (9): 1243. https://doi.org/10.3390/cryst12091243.

Zakirov, A., S. Belousov, M. Bogdanova, B. Korneev, A. Stepanov, A. Perepelkina, V. Levchenko, A. Meshkov, and B. Potapkin. 2020. "Predictive Modeling of Laser and Electron Beam Powder Bed Fusion Additive Manufacturing of Metals at the Mesoscale." *Additive Manufacturing* 35:101236. https://doi.org/10.1016/j.addma.2020.101236.

Zhang, B., Y. Li, and Q. Bai. 2017. "Defect Formation Mechanisms in Selective Laser Melting: A Review." *Chinese Journal of Mechanical Engineering* 30 (3): 515–527. https://doi.org/10.1007/s10033-017-0121-5.

Zhao, C., N. D. Parab, X. Li, K. Fezzaa, W. Tan, A. D. Rollett, and T. Sun. 2020a. "Critical Instability at Moving Keyhole Tip Generates Porosity in Laser Melting." *Science* 370 (6520): 1080–1086. https://doi.org/10.1126/science.abd1587.

Zhao, C., N. D. Parab, X. Li, K. Fezzaa, W. Tan, A. D. Rollett, and T. Sun. 2020b. "Critical Instability at Moving Keyhole Tip Generates Porosity in Laser Melting." *Science* 370 (6520): 1080–1086. https://doi.org/10.1126/science.abd1587.

Zheng, H., H. Li, L. Lang, S. Gong, and Y. Ge. 2018. "Effects of Scan Speed on Vapor Plume Behavior and Spatter Generation in Laser Powder Bed Fusion Additive Manufacturing." *Journal of Manufacturing Processes* 36:60–67. https://doi.org/10.1016/j.jmapro.2018.09.011.

Zu, Y. Q., and S. He. 2013. "Phase-Field-Based Lattice Boltzmann Model for Incompressible Binary Fluid Systems with Density and Viscosity Contrasts." *Physical Review E* 87 (4): 043301. https://link.aps.org/doi/10.1103/PhysRevE.87.043301.

Appendix A. Model details

A.1 *Phase Field Model*

Solidification and grains grow process is modeled using phase-field method. The formulation follows the approach proposed by Moelans *et al*. (Chatterjee and Moelans 2021; Heulens, Blanpain, and Moelans 2011; Moelans, Blanpain, and Wollants 2008). The method introduces the multidimensional order parameter

$$\overline{\phi} = \left[\phi_l, \phi_{g_1} \ldots, \phi_{g_N}\right]. \tag{A1}$$

where ϕ_l and ϕ_{g_i} describe liquid phase and individual grains, respectively. The number of allowed grain orientations is set to some large number (10^4 in this work). $\overline{\phi}$ evolves by minimizing the free energy

$$F = \int \left[Wg + \frac{K}{2} \sum_i (\quad \phi_i)^2 + f_{tr} \right] dV. \tag{A2}$$

where the bulk component g is defined within Moelans *et al*. formulation by

$$g = \sum_i \left(\frac{\phi_i^4}{4} - \frac{\phi_i^2}{2} \right) + \frac{3}{2} \sum_{i<j} \phi_i^2 \phi_j^2 + \frac{1}{4}. \tag{A3}$$

The parameters W and K are interface sensitive and defined as

$$W = \frac{\sum_{i<j} W_{ij} \phi_i^2 \phi_j^2}{\sum_{i<j} \phi_i^2 \phi_j^2} \tag{A4}$$

$$K = \frac{\sum_{i<j} K_{ij} \phi_i^2 \phi_j^2}{\sum_{i<j} \phi_i^2 \phi_j^2}, \tag{A5}$$

where $W_{ij} = \frac{3\sigma_{ij}}{4\Delta}$ and $K_{ij} = 6\sigma_{ij}\Delta$. σ_{ij}, and Δ are the energy and width of the interface. The component f_{tr} is introduced to drive the solid-liquid phase transition

$$f_{tr} = \sum_i G_i h_i, \tag{A6}$$

where G_i is the free energy of a particular phase and h_i are the phase fractions defined using components of order parameter vector

$$h_i = \frac{\phi_i^2}{\sum_i \phi_i^2}. \tag{A7}$$

All grains are in relative equilibrium and their corresponding free energy is set to zero ($G_g = 0$) and considered as the reference. In such case, G_l can be related to the latent heat of fusion L and the melting temperature T_m

$$G_l = -\frac{L}{T_m}(T - T_m). \tag{A8}$$

The components of $\overline{\phi}$ evolve as non-conserved fields,

$$\frac{\partial \phi_i}{\partial t} = -\Gamma \mu_i, \tag{A9}$$

where $\mu_i = \frac{\partial F}{\partial \phi_i}$. Γ determines the rate of solid–liquid transition, similarly to W and K, it is interface sensitive:

$$\Gamma = \frac{\sum_{i<j} \Gamma_{ij} \phi_i^2 \phi_j^2}{\sum_{i<j} \phi_i^2 \phi_j^2},$$

where Γ_{ij} is the interface mobility.

In the above formulation, the phase transition between solid and liquid is initiated by the nucleation. A corresponding fluxes of liquid and solid phase are defined (Dong and Lee 2005; Gandin, Rappaz, and Tintillier 1994) as follows.

$$j_l(\Delta T) = -j_g(\Delta T)$$

$$j_I(\Delta T) = \frac{j_{max}}{\sqrt{2\pi}\Delta T_\sigma} \int_0^{\Delta T} \exp\left(-\frac{1}{2}\left(\frac{\Delta T - \Delta T_N}{\Delta T_\sigma}\right)^2\right) d(\Delta T). \tag{A10}$$

The average under-cooling temperature ΔT_N and its standard deviation ΔT_σ are the input parameters, while j_{max} is proportional to density of nucleation centers. The grain evolution does not affects the conclusions presented in this work; therefore, for simplicity, the nucleation is active only in solid phase at the melting and the grains epitaxially.

Grain growth anisotropy is introduced using orientation-dependent grain/liquid interfacial mobility (Radhakrishnan et al. 2019; Steinbach 2009)

$$\tilde{\Gamma}_{lg} = \Gamma_{lg}(1 - 3\delta)\left[1 + \frac{4\delta}{1 - 3\delta}\left\{\left(n_x^{'}\right)^4 + \left(n_y^{'}\right)^4 + \left(n_z^{'}\right)^4\right\}\right], \tag{A11}$$

where δ is an anisotropy parameter, $\mathbf{n}^{'} = \mathbf{Rn}$, where $\mathbf{n} = \left.\phi_g\right| \left.\phi_g\right|$ is normal direction to the grain/liquid interface, $\mathbf{R}$ is the rotation matrix from global to local frame constructed in the following way:

$$\mathbf{R} = \mathbf{BCD} \tag{A12}$$

$$\mathbf{D} = \begin{bmatrix} \cos\alpha & \sin\alpha & 0 \\ -\sin\alpha & \cos\alpha & 0 \\ 0 & 0 & 1 \end{bmatrix}, \mathbf{C} = \begin{bmatrix} 1 & 0 & 1 \\ 0 & \cos\beta & \sin\beta \\ 0 & -\sin\beta & \cos\beta \end{bmatrix},$$

$$\mathbf{B} = \begin{bmatrix} \cos\gamma & \sin\gamma & 0 \\ -\sin\gamma & \cos\gamma & 0 \\ 0 & 0 & 1 \end{bmatrix} \tag{A13}$$

where polar angles defining grain orientation are $\alpha = 2\pi x$, $\beta = \arccos(2y - 1)$, $\gamma = 2\pi z$, with x, y, z randomly generated from $[0, 1]$.

A.2. *Thermal Solver*

The temperature field is evaluated by solving the heat diffusion equation within the region occupied by the solid or liquid phases with periodic boundary conditions in the lateral directions.

$$\cdot \kappa \quad T + \dot{q} = \rho c_p \frac{\partial T}{\partial t}, \tag{A14}$$

where ρ, κ and c_p are the material density, heat conductivity and heat capacity, respectively. $\dot{q}$ represents combined source term

$$\dot{q} = \dot{q}_l + \dot{q}_c + \dot{q}_r + \dot{q}_v + \dot{q}_f, \tag{A15}$$

where $\dot{q}_l$ captures the effect of laser beam, in this work modeled explicitly by ray tracing (Cho and Na 2006; Tan, Bailey, and Shin 2013). For that purpose, 10^4 rays are randomly distributed following Gaussian distribution, with 4σ being equal to beam diameter. $\dot{q}_c$ in Eq. A15 represents the convection term accounting for the heat transfer through the bottom surface of the RVE and the heat exchange with chamber atmosphere at the interface of solid or liquid with vapor,

$$\dot{q}_c = -C_b(T - T_b), \tag{A16}$$

where C_b is the convection coefficient and T_b is the temperature of the material or gas surrounding the RVE. $\dot{q}_r$ represents radiation cooling

$$\dot{q}_r = -C_r\sigma\left(T^4 - T_b^4\right), \tag{A17}$$

where C_r is the black-body constant. The vaporization cooling ($\dot{q}_v$) follows Anisimov recoil model,

$$\dot{q}_v = -\frac{1}{\sqrt{2\pi R_g T}} p_r L_v \exp\left(\frac{L_v}{R_g}\left(\frac{1}{T_v} - \frac{1}{T}\right)\right), \tag{A18}$$

where p_r is the reference pressure, R_g is the gas constant, T_v is the vaporization temperature, L_v is the latent heat of vaporization. $\dot{q}_f$ is contribution from the latent heat of fusion due to the solid/liquid transformation,

$$\dot{q}_f = \frac{\partial h_l}{\partial t}\Big|_{g \leftrightarrow l} L_f, \tag{A19}$$

where h_l is liquid phase fraction and L_f is the latent heat of fusion. Similarly to vaporization cooling, temperature change due to this term is not allowed to cross melting temperature, limiting the value of phase change flux.

A.3. *Melt pool dynamics*

The melt pool flow solver implements the Lattice Boltzmann Method (LBM) (Krüger et al. 2017) for incompressible flow formulated by Guo *et al*. (Z. Guo, Shi, and Wang 2000). In BGK approximation, the distribution functions are propagated using following equation

$$f_a(\mathbf{x}+\mathbf{e}_a, t+1) = f_a(\mathbf{x},t) - \frac{f_a - f_a^{eq}}{\tau + 1/2} + \frac{\tau}{\tau+1/2}\omega_a\left(\mathbf{e}_a/c_s^2\right)\cdot\mathbf{F}/\rho, \tag{A20}$$

where the time step and and grid spacing were set to 1. $\tau = \nu/c_s^2\Delta t$ is the relaxation time. f^{eq} are the equilibrium distribution functions (Z. Guo, Shi, and Wang 2000; Zu and He 2013)

$$f_a^{eq} = \begin{cases} -(1-\omega_0) - \omega_0\frac{u^2}{2c_s^2}, & a = 0 \\ \omega_a\left[\frac{p}{c_s^2} + \frac{\mathbf{e}_a\cdot\mathbf{u}}{c_s^2} + \frac{(\mathbf{e}_a\cdot\mathbf{u})^2}{2c_s^4} + \frac{u^2}{2c_s^2}\right]. & a \neq 0 \end{cases}, \tag{A21}$$

discretized over d3q19 velocity set

$$\mathbf{e}_{0-4} = \begin{bmatrix} 0 & 1 & 0 & 0 & -1 & 0 & 0 \\ 0 & 0 & 1 & 0 & 0 & -1 & 0 \\ 0 & 0 & 0 & 1 & 0 & 0 & -1 \end{bmatrix} \tag{A22}$$

$$\mathbf{e}_{5-18} = \begin{bmatrix} 1 & -1 & 1 & -1 & 1 & -1 & -1 & 1 & 0 & 0 & 0 & 0 \\ 1 & -1 & -1 & 1 & 0 & 0 & 0 & 0 & 1 & -1 & 1 & -1 \\ 0 & 0 & 0 & 0 & 1 & -1 & 1 & -1 & 1 & -1 & -1 & 1 \end{bmatrix},$$

with the weight coefficients

$$\omega_a = \begin{cases} 1/3 & a = 0 \\ 1/18 & a = 1,\ldots,6 \\ 1/36 & a = 7,\ldots,18. \end{cases}. \tag{A23}$$

This work implements two-relaxation time (TRT) approximation, which offers improved numerical stability (Ginzburg, Verhaeghe, and d'Humiéres 2008 b; d'Humières and Ginzburg 2009; Ginzburg, Verhaeghe, and d'Humiéres 2008 a) over single-relaxation scheme without loosing computational efficiency. TRT approximation propagates the distribution functions using positive and negative linear combinations of Eq. A20, leading to separate equations for f_a^+ and f_a^- with equilibrium functions f_a^{eq+} and f_a^{eq-}

$$\begin{aligned} f_a^+ &= (f_a + f_{\bar{a}})/2, & f_a^- &= (f_a - f_{\bar{a}})/2 \\ f_a^{eq+} &= \left(f_a^{eq} + f_{\bar{a}}^{eq}\right)/2, & f_a^{eq-} &= \left(f_a^{eq} - f_{\bar{a}}^{eq}\right)/2. \end{aligned}. \tag{A24}$$

and f_a^+ is propagated with τ^+, f_a^- is propagated with τ^-

$$\tau^+ = \tau = \nu/c_s^2\Delta t \tag{A25}$$

$$\tau^- = \Lambda/\tau^+\Delta t^2, \tag{A26}$$

where $\Lambda = 1/4$.

Considering liquid/vapor interface, the implementation follows volume of fluid (VOF) approach (Körner et al. 2005), where the melt interface is treated as a free surface. Within VOF approach, the grid-point cells are divided into three categories: 'bulk', 'interface' and 'vapor'. By definition, the 'interface' cells separate 'bulk' and 'vapor' cells. The melt pool/vapor interface is moved by changing the occupancy of the 'interface' cells. If the occupancy drops below zero, the cell becomes 'vapor' cell and the neighboring 'bulk' cell becomes an 'interface'. Similarly, if an occupancy of the 'interface' gets higher than one, it becomes 'bulk' and a neighboring 'vapor' cell becomes an interface. The rate at which the interface cells change occupancy is determined by projection of the fluid velocity at the normal to the interface:

$$j_l^{LBM} = \mathbf{u}\cdot\mathbf{n}. \tag{A27}$$

The force (F) in Eq. A20 accounts for the effect of surface tension ($\mathbf{F}_s$), recoil pressure ($\mathbf{F}_r$), Marangoni ($\mathbf{F}_M$) force, local pressure at free surface ($\mathbf{F}_p$) and gravity ($\mathbf{F}_g$).

$$\mathbf{F} = \mathbf{F}_s + \mathbf{F}_r + \mathbf{F}_M + \mathbf{F}_p + \mathbf{F}_g \tag{A28}$$

$$\mathbf{F}_s = -(\sigma \quad \cdot\mathbf{n})\mathbf{n} \tag{A29}$$

$$\mathbf{F}_r = \left(0.54 p_r \exp\left[\frac{L_v}{R_g}\left(\frac{1}{T_v} - \frac{1}{T}\right)\right]\right)\mathbf{n} \tag{A30}$$

$$\mathbf{F}_M = C_M[\ \ T - (\mathbf{n}\cdot\ \ T)\mathbf{n}] \tag{A31}$$

$$\mathbf{F}_p = -P_b\mathbf{n} \tag{A32}$$

$$\mathbf{F}_g = -g\hat{z} \tag{A33}$$

where σ is the surface tension, C_M is the Marangoni constant, p_r is the recoil reference pressure, L_v is the vaporization latent heat, T_v is the boiling temperature, and g is the gravity constant. P_b is a gas pressure at the interface, equal to the chamber pressure in a case the interface faces the chamber. For enclosed pores inside the melt pool, we engage a tracking algorithm that detects pores, evaluates their volumes, gas temperature, and pressure assuming ideal gas state equation.

The LBM solver is active within the melt pool domain, determined by condition

$$h_l > L_l, \tag{A34}$$

where L_l is the minimal amount of liquid fraction in the melt pool. L_l can be set between 0 and 1; in this work it is set to 10^{-3}. Considering boundary conditions on the vapor side, the missing components of the distribution functions are reconstructed using a simple anti-bounce-back scheme commonly used to model flow with free surface (Körner et al. 2005, Chen, Teixeira, and Molvig 1998). On the solid side of the boundary, a simple bounce-back method (Ladd 1994, He et al. 1997) is used to reconstruct the unknown distribution function incoming from the solid side of the melt pool boundary. Alongside the bounce-back scheme, the immersed boundary conditions are implemented as proposed by Noble and Torczynski (Noble and Torczynski 1998) and modified by Strack and Cook (Strack and Benjamin 2007).

Appendix B. Model and material parameters

The implementation follows the explicit scheme with time step $\Delta t = 5 \times 10^{-8} s$ and uniform grid with spacing $\Delta x = 5 \times 10^{-6} m$. The material of choice is Ni-based super alloy IN718. All respective material and model parameters are gathered in the Table B1.

Table B1. Material and model parameters for IN718.

thermal solver			
property	symbol	units	value
material density	ρ	kg/m^3	8440
specific heat	c_p	J/kgK	440
heat conductivity	κ	W/mK	60
cooling factor Bottom	C_b	-	10^{-2}
convection heat transfer coefficient	C_t	Wm^2K	50
absorptivity	A	-	0.7
heat source radius (2σ)	R_L	m	5×10^{-5}
latent heat vaporization	L_v	J/kg	5.49×10^6
latent heat formation	L_f	J/kg	2.819×10^5
melting temperature	T_v	K	1533.15
boiling temperature	T_m	K	3174
phase solver			
interfacial energy (solid/liquid)	σ_{lg}	N/m	0.17
interfacial width	Δ	m	10^{-5}
interfacial mobility (liquid lquid/solid)	Γ_{lg}	m^3/sJ	10^{-3}
grain anisotropy parameter	δ	-	0.2
nucleation undercooling	ΔT_N	K	20
nucleation undercooling	ΔT_σ	K	8
nucleation amplitude	j_{max}	$1/m^3 s$	10^{19}
LBM			
surface tension	σ	N/m	1.7
Marangoni force coefficient	C_M	N/mK	-2.8147×10^{-4}
recoil reference pressure	p_r	pa	5.371×10^4

Appendix C. Implementation details

Due to the size of the RVE (see Figure 1), all calculations have been performed on a computing cluster using 256 cores (2 nodes each containing 2 AMD EPYC-Milan processors 64 core each). The RVE is represented by 600 $\times$ 150 $\times$ 200 mesh (5 μm grid size). The actual number of time steps necessary to complete a simulation depends on the scan speed, but including cooling stage, this may vary between 25 and 50×10^3. The slowest calculation takes no more than 20 hours to complete. The code is parallelized using Message Passing Interface (MPI) implementing the "envelope approach" within Cartesian communicator. In such approach, each process holds its share of distributed fields and in addition a layer that belongs to its neighbor such that gradient operation can be performed for any grid point in the process domain. The shared layer of the data (envelope) must be synchronized between processes after each time the data is modified, triggering send/receive MPI functions.